IEEE Access
Multidisciplinary | Rapid Review | Open Access Journal

Received August 31, 2020, accepted September 9, 2020, date of publication September 14, 2020,
date of current version September 24, 2020.

Digital Object Identifier 10.1109/ACCESS.2020.3023690

Transparency Estimation of Narrow Rivers by UAV-Borne Hyperspectral Remote Sensing Imagery

LIFEI WEI[1,2,3], ZHOU WANG[1], CAN HUANG[1], YU ZHANG[1], ZHENGXIANG WANG[1,2], HUIQIONG XIA[1], AND LIQIN CAO[4], (Member, IEEE)

[1]Faculty of Resources and Environmental Science, Hubei University, Wuhan 430062, China
[2]Hubei Key Laboratory of Regional Development and Environmental Response, Hubei University, Wuhan 430062, China
[3]Key Laboratory of Urban Land Resources Monitoring and Simulation, MNR, Shenzhen 518034, China
[4]School of Printing and Packaging, Wuhan University, Wuhan 430079, China

Corresponding author: Zhou Wang (wangzhou_rs@163.com)

This work was supported in part by the "National Key Research and Development Program of China" under Grant 2019YFB2102902 and Grant 2017YFB0504202, in part by the " Natural Science Foundation Key projects of Hubei Province" under Grant 2020CFA005, in part by the "Open Fund of Key Laboratory of Urban Land Resources Monitoring and Simulation, MNR", under Grant KF-2019-04-006, in part by the "National Natural Science Foundation of China" under Grant 41622107, in part by the "central government guides local science and technology development projects" under Grant 2019ZYYD050, in part by the "Special projects for technological innovation in Hubei" under Grant 2018ABA078, in part by the "Open Fund of Key Laboratory of Ministry of Education for Spatial Data Mining and Information Sharing" under Grant 2018LSDMIS05, in part by the "Open Fund of the State Laboratory of Information Engineering in Surveying, Mapping, and Remote Sensing, Wuhan University" under Grant 18R02, and in part by the "Open fund of Key Laboratory of Agricultural Remote Sensing of the Ministry of Agriculture" under Grant 20170007.

ABSTRACT Urban rivers are often narrow, and general remote sensing data cannot meet the needs of water quality monitoring. In the process of monitoring of river water quality by remote sensing, the spectral and spatial dimension of satellite-borne images cannot be taken into consideration at the same time, making fine pollution monitoring of urban rivers difficult. Transparency is one of the core indicators for evaluating water quality, and hyperspectral remote sensing data are rich in spectral information and can be used for quantitative transparency estimation. The application of unmanned aerial vehicles (UAV)remote sensing effectively makes up for the deficiencies in satellite remote sensing monitoring. Aiming at this problem, this paper proposed the use of the eXtreme Gradient Boosting (XGBoost) regression algorithm for the quantitative inversion of urban river transparency. The spatial resolution of the collected imagery is 18.5 cm, which is suitable for urban rivers that are almost ten meters wide. Compared with five traditional empirical models, integrated algorithms such as gradient regression and random forest get much better results. Moreover, the accuracy of transparency estimation using the XGBoost regression algorithm was significantly improved, and the inversion model R^2 in both study areas reached over 0.97. Finally, the established transparency inversion models were used to generate transparency distribution maps of the two study areas. The results showed that the distribution of the water transparency was consistent with the results of the field monitoring, indicating that it is feasible to use the XGBoost algorithm for the inversion of urban river transparency in UAV-borne hyperspectral imagery.

INDEX TERMS Transparency, UAV-borne, extreme gradient boosting, hyperspectral imagery.

I. INTRODUCTION

Water resources are vital for human reproduction and life, and provide an irreplaceable ecological function [1], [2]. With the rapid development of the economy, human activities have intensified and had a series of impacts on the environment [3], [4]. The reasonable protection, development, and utilization of water resources are important aspects for the protection and sustainable development of the ecological environment [5]. Therefore, the need for accurate water quality monitoring is becoming increasingly urgent. Water transparency is very important in water ecology because it

The associate editor coordinating the review of this manuscript and approving it for publication was Xujie LI.

This work is licensed under a Creative Commons Attribution 4.0 License. For more information, see https://creativecommons.org/licenses/by/4.0/

directly affects the depth that light can penetrate [6], [7], and is related to the spatial distribution of benthic plants such as large algae [8]. At certain water depths, the areas with higher transparency tend to have more vegetation. In contrast, in the areas with lower transparency, many aquatic plants cannot photosynthesize, because of the insufficient light. In addition, transparency is also related to planktonic algae, colored dissolved organic matter (CDOM), and suspended particles in the water [9]. Transparency is also a core indicator for evaluating the eutrophication of water bodies [10]. Therefore, it is of great significance to accurately monitor the transparency of water bodies.

Water transparency can be measured by optical sensors (such as transmissometers) and Secchi disks [11]. The Secchi disk, in particular, is widely used to indicate the transparency of water, in part because it is convenient, cheap and easy to obtain. Due to the spatial heterogeneity of water quality distribution, remote sensing technology can accurately, quickly, and effectively cover large areas [12], [13], and can obtain data that are difficult to obtain manually. As a result, remote sensing has become the most popular data source for obtaining regional-scale water body transparency data [14].

With regard to the remote sensing estimation of water body transparency, scholars have done a lot of research, but the research objects are mostly sea areas, rivers, and large lakes, and the data used are mostly space-borne data [4], [7], [15]–[18]. For example, Setiawan *et al.* [19] used Landsat imagery to estimate long-term lake transparency changes. For airborne hyperspectral data, Thiemann and Kaufmann [20] used airborne hyperspectral data to monitor the transparency of Mecklenburg Lake in Germany. Many scholars use various data to monitor the transparency of water bodies, such as TM [21], MSS [22], IKONOS [23] and even video data [24]. Among them, Landsat data is more widely used, and its single band or band ratio is used to build the transparency measurement algorithm, which has good performance [25]. These researches are aimed at larger scale water body transparency measurements. However, for the transparency monitoring of urban narrow river channels, the spatial and spectral resolutions of the traditional space-borne or airborne remote sensing data cannot meet the accurate monitoring requirements [26].

Unmanned aerial vehicle (UAV)-borne hyperspectral remote sensing images have high spatial and spectral resolutions, and are being used more and more in ecological monitoring [27]. At the same time, UAV-drones have many advantages such as low cost, low loss, reusability and easy operation, which can provide powerful help for environmental monitoring and effectively improve the quality of environmental monitoring. In this study, we applied a UAV remote sensing platform equipped with a miniature hyperspectral sensor to obtain hyperspectral remote sensing image data, which were combined with ground-based measured data, and used eXtreme Gradient Boosting (XGBoost) machine learning algorithm for urban river channel transparency monitoring. The purpose of this study was to combine UAV-borne hyperspectral imagery with a machine learning algorithm, and provide a reference for urban river channel transparency monitoring research.

II. MATERIALS AND METHODS

A. STUDY AREAS

Two inland channels in Wuhan, China, were selected as the experimental areas for this study. The Shahu Port channel (114° 21' 22.36'' E, 30° 35' 11.44'' N) is one of Wuhan's many port channels, running from Youyi Avenue in the northeast, to Waisha Lake in the southwest, and Donghu Lake in the southeast. The port channel merges with the Yangtze River and has a total length of about 9.45 km. It is an important channel connecting Donghu Lake and Shahu to the Yangtze River. Due to the poor drainage and environmental conditions, the Shahu Port channel is a typical polluted urban water body. At the time of writing, the black odorous water treatment project at Shahu Port has now been completed, as has a dredging project. However, the water bodies of Shahu Port have been contaminated for a long time, and the problem of low visibility still exists. The selected study area of the port channel runs from Yangyuan South Road to Luojiagang Interchange, in which 40 sampling points are evenly distributed.

The Xunsi River (114° 18' 0.12'' E, 30° 29' 58.87'' N) is 16 km long and is located in the southern part of Wuhan City. It flows through Jiangxia District, Hongshan District, and Wuchang District, and finally joins the Yangtze River. With the continuous discharge of untreated domestic sewage into the river, the water body is now seriously polluted. There are many floating objects in the river, and the water quality is very poor. The river is gray-black in color and has an unpleasant odor. The pollution degree of the water body is greater than that of the Shahu Port channel. The research area covers a section of U-shaped river, in which 32 sampling points are evenly arranged in the river channel.

B. DATA COLLECTION

The data collected in this study included the transparency of the river sampling points, latitude and longitude coordinates, and measured ground spectra. A JCT-8 Secchi disk was used for the transparency field measurement. To ensure the accuracy of the measurement results, each measurement was repeated two to three times.

The ground-based measurement of the spectrum of the water was undertaken based on the ''above-water surface method'' [28]. When collecting the ground-based spectrum, calibration was first achieved on a standard board, the water surface spectrum was then recorded, and finally the spectrum of the sky was also collected. In the acquisition process, care was taken to avoid direct sunlight; otherwise, the instrument would be overexposed, resulting in unusable sampling data.

C. UAV-BORNE IMAGE ACQUISITION AND PREPROCESSING

The hyperspectral imagery was obtained with a Nano-HyperSpec mini hyperspectral imager. As shown in Table 1,

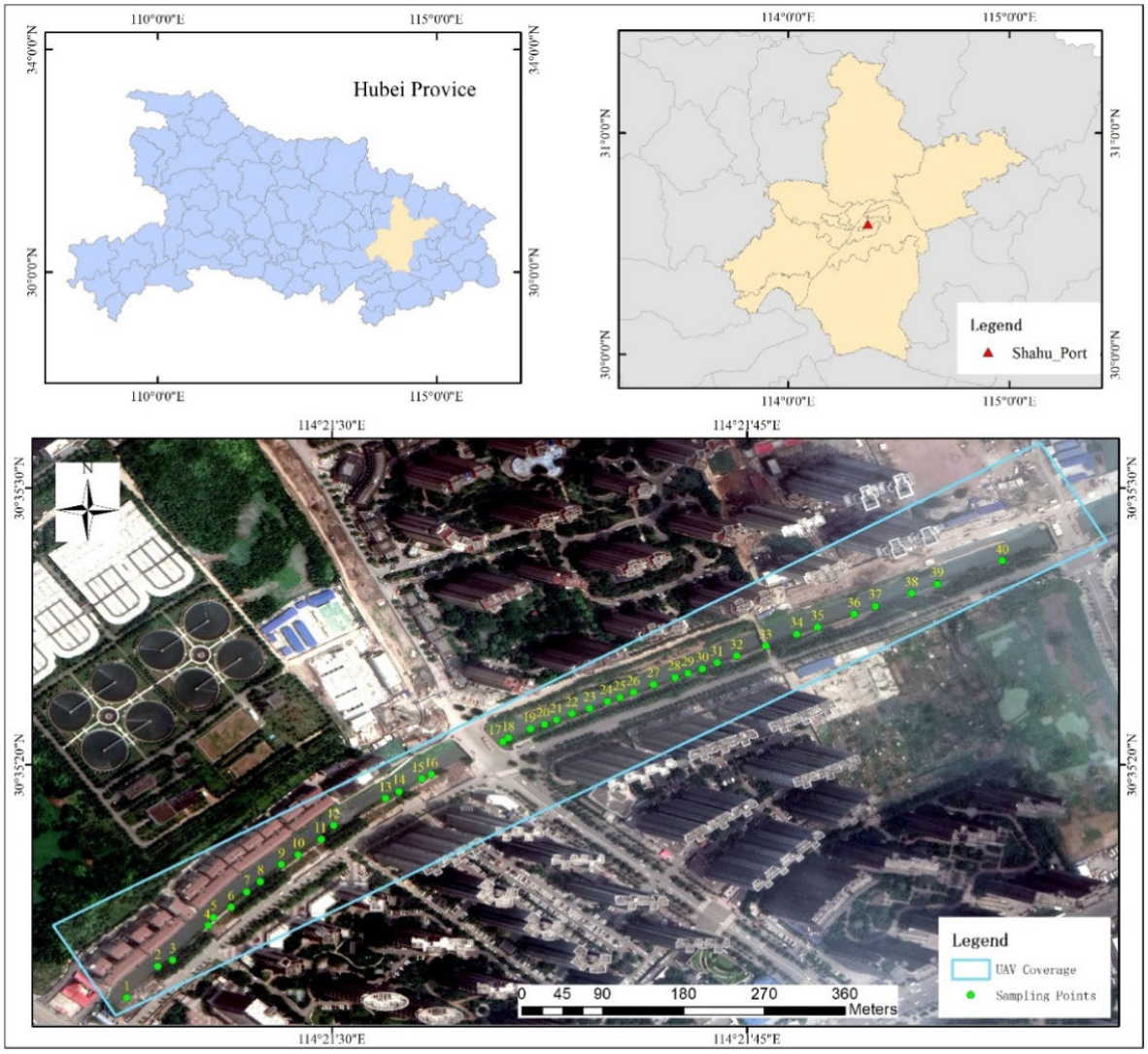

FIGURE 1. Sampling points in the Shahu Port channel.

the wavelength range of the Nano-HyperSpec sensor is 400–1000 nm, the number of spectral channels is 270, and the number of spatial channels is 640. The global positioning system/inertial measurement unit (GPS/IMU) module records the attitude information of the imager (including altitude, longitude, latitude, roll, pitch, and yaw). After loading the attitude information into the post-processing software provided by Headwall, the user can geometrically correct the collected strips. In addition, each Nano-HyperSpec sensor is calibrated with a lens selected by the user before it leaves the factory. The radiation can be directly corrected in the post-processing software provided by Headwall to convert the digital number (DN) data into radiance data. Coaxial reflection spectrum imaging technology is adopted, which has the advantages of a compact size and accurate spectral information. The hyperspectral data collection was performed on May 31 and June 1, 2019, at the Shahu Port channel and the Xunsi River, respectively. The flight platform for the

TABLE 1. Flight parameters of the sensor and UAV.

Class	Parameter	Class	Parameter
Wavelength range	400–1000 nm	Flight height	200 m
Number of spectral channels	270	Spatial resolution	18.5 cm
Number of spatial channels	640	UAV type	DJI M600 Pro

Nano-HyperSpec hyperspectral imaging system was a six-rotor DJI M600 Pro drone. The flight altitude was set to 200 m. The spatial resolution of the collected imagery is 18.5 cm, the wavelength range is 0.4–1um, and the number of spectral bands is 270.

The UAV-borne hyperspectral data processing consisted of sensor radiation calibration, site radiation correction,

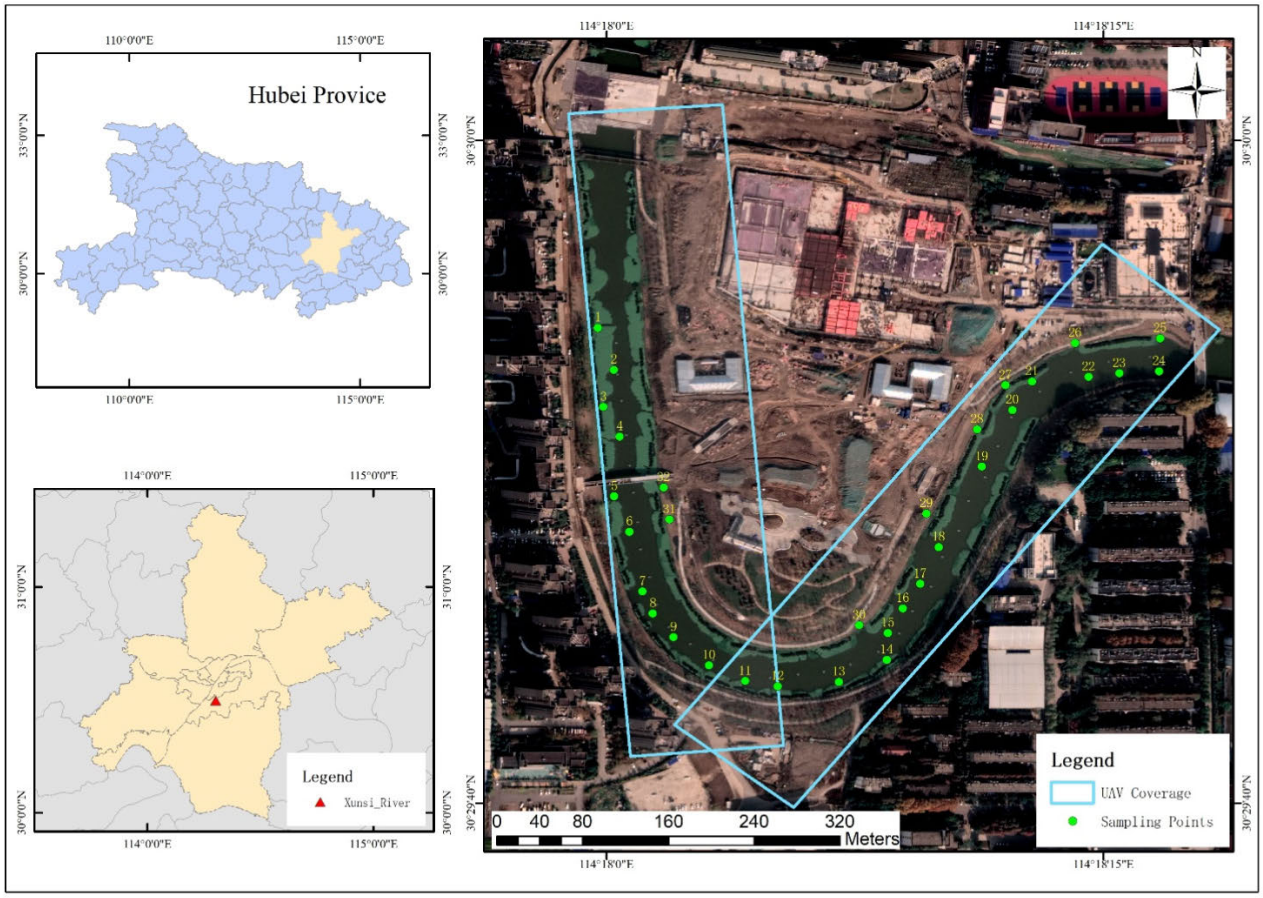

FIGURE 2. Sampling points in the Xunsi river channel.

geometric correction, and water extraction. Sensor radiation calibration involves converting the signal output by the sensor unit into the actual radiation intensity value. In this study, according to the radiation correction model and the conversion parameters provided by the sensor manufacturer, the original image data were converted pixel-by-pixel from the DN value to the radiance value. The remote sensing reflectance of the off-water radiation from the ground sampling point and the geometrically corrected remote sensing image pixel spectrum were then used to construct a linear relationship between the airborne radiation curve and the ground measured spectrum, so as to achieve site radiation correction. Because the drone was flown at a height of only 200 m, the complex atmospheric effects could be ignored. The image information was also geometrically corrected with the GPS/IMU module's attitude information [29].

III. METHODS

A. EXTREME GRADIENT BOOSTING

Integrated learning involves building and combining multiple learners to complete the learning task. By combining multiple learners, it is often possible to obtain a significantly better generalization performance than with a single learner, so this approach is widely used in water quality monitoring [30]. The eXtreme Gradient Boosting (XGBoost) algorithm is a typical representative of the integrated algorithms, which was proposed in 2016, based on a regression tree [31]. XGBoost is a massively parallel boosted tree tool. The regression tree and the decision tree are similar in concept, and they are both tree-based algorithms.

The basis of XGBoost is the gradient boosting algorithm. Gradient boosting is a powerful technique for building predictive models. The integrated algorithm builds multiple weak evaluators on the data set and summarizes the modeling results of all the weak estimators to obtain a better regression or classification performance than with a single model. A weak evaluator is defined as a model that performs at least better than random guessing, that is, any model with a prediction accuracy of not less than 50%.

There are many ways to integrate the different weak evaluators. One approach is a bagging method that builds multiple parallel and independent weak evaluators at one time. Its typical representative method is the random forest algorithm [32]. Another approach is the lifting method, whose principle is to build weak evaluators one by one and gradually accumulate the multiple weak estimators after multiple iterations [33].

The most famous algorithms based on the lifting method are AdaBoost [34] and the gradient boosting decision tree (GBDT) [35]. XGBoost was developed from GBDT. There can be regression trees or classification trees in the gradient boosting tree structure, both of which use the classification and regression tree (CART) algorithm as the mainstream tree structure. The gradient lifting regression tree is an integrated model focusing on the regression tree model. Its modeling process is as follows. Firstly, a tree is built and then iterated gradually. A tree is added during each iteration, and a strong evaluator integrated with the many tree models is gradually formed.

For XGBoost, each leaf node will have a prediction score, which is also known as the leaf weight. This leaf weight is the regression value of all the samples on this leaf node on this tree, and is expressed by (x_i) or w, where f_k represents the kth decision tree and x_i represents the feature vector corresponding to sample i. When there is only one tree, $f_1(x_i)$ is the result returned by the lifting algorithm, but this result is far from ideal. When there are multiple trees, the regression result of the integrated model is the sum of the predicted scores of all the trees. Assuming that there are k decision trees in the integrated model, then the prediction results given by the entire model on sample i are:

$$\hat{y}_i^{(k)} = \sum_{\mathrm{K}}^{k} f_k(x_i) \tag{1}$$

where $\hat{y}_i^{(k)}$ represents the predicted value of the ith sample transparency in this experiment, and x_i represents the input sample.

Accurate prediction is a very important factor, and XGBoost implements an algorithm that balances model performance and operation speed. The common loss functions, such as error rate and mean-square error, can only measure the performance of the model and cannot measure the speed of the model. Spatial complexity and temporal complexity are used in many models to measure the computational efficiency of the model. Therefore, XGBoost introduces model complexity to measure the algorithm's operational efficiency, the formula of which is expressed as:

$$obj(\theta) = \sum_{i}^{n} L(y_i, \hat{y}_i) + \sum_{k=1}^{K} \Omega(f_k) \tag{2}$$

where i represents the ith sample in the data set, n represents the total amount of data imported into the kth tree, and K represents all the established trees. The first term represents the traditional loss function, which measures the difference between the true value and the predicted value. The measured difference is usually the adjusted standard error. The second term represents the complexity of the model, which is represented by a transformation of the tree model. This change represents a formula for measuring the complexity of the tree model from the structure of the tree, which is defined as follows:

$$\Omega(f) = \gamma T + \frac{1}{2}\lambda \|w\|^2 \tag{3}$$

where T is the number of leaf nodes and $\|w\|$ is the modulus of the leaf node vector. γ represents the difficulty of the node segmentation and λ represents the L2 regularization coefficient. In the process of iterating each tree, it is minimized in an attempt to obtain the optimal result, so the model error rate and model complexity are minimized at the same time.

According to (2), the objective function of the learning model for a total of t iterations is:

$$\begin{aligned} obj^{(t)} &= \sum_{i=1}^{n} L(y_i, \hat{y}_i^{(t)}) + \sum_{k=1}^{t} \Omega(f_k) \\ &= \sum_{i=1}^{n} L(y_i, \hat{y}_i^{(t-1)} + f_t(x_i)) + \sum_{k=1}^{t-1} \Omega(f_k) + \Omega(f_t) \end{aligned} \tag{4}$$

According to Taylor's second-order approximate expansion,

$$obj^{(t)} = \sum_{i=1}^{n} [g_i \cdot f_t(x_i) + \frac{1}{2} h_i \cdot f_t(x_i)^2] + \Omega(f_t) + C \tag{5}$$

where:

$$\begin{aligned} g_i &= \partial_{\hat{y}^{(t-1)}} l(y_i, \hat{y}^{(t-1)}) \\ h_i &= \partial^2_{\hat{y}^{(t-1)}} l(y_i, \hat{y}^{(t-1)}) \end{aligned} \tag{6}$$

where $l(y_i, \hat{y}^{(t-1)})$ represents the prediction error of the learning model composed of the previous $t-1$ trees. g_i and h_i represent the first and second derivatives of the prediction model for the current model, respectively. The current model iterates in the direction of decreasing prediction error.

By combining (1) and (3), ignoring the constant terms, the structure of the tree introduced into the loss function, and the objective function will continue to transform. The purpose of transforming the objective function is to establish a direct relationship between the structure of the tree (the number of leaf nodes) and the size of the objective function, in order to find the optimal tree f_t that needs to be solved in the tth iteration, to obtain:

$$obj^{(t)} = \sum_{j=1}^{T} [G_j w_j + \frac{1}{2}(H_j + \lambda) w_j^2] + \gamma T \tag{7}$$

where:

$$\sum_{i \in I_j} g_i = G_j, \quad \sum_{i \in I_j} h_i = H_j \tag{8}$$

Find the optimal weight:

$$w_j^* = -\frac{G_j}{H_j + \lambda} \tag{9}$$

Bring in the objective function and obtain the optimal solution of the objective function:

$$obj^* = -\frac{1}{2} \sum_{j=1}^{T} \frac{G_j^2}{H_j + \lambda} + \gamma T \tag{10}$$

Equation (10) is a function for scoring a tree structure, where the smaller the score, the better the tree structure. The algorithm searches for the optimal tree structure by constructing different tree structures using (10). All the segmentation points of the sample features are first determined, and each identified segmentation point is segmented. The criteria for the segmentation are as follows:

$$Gain = \frac{1}{2}\left[\frac{G_L^2}{H_L+\lambda} + \frac{G_R^2}{H_R+\lambda} - \frac{(G_L+G_R)^2}{H_L+H_R+\lambda}\right] - \gamma \quad (11)$$

where *Gain* represents the difference between the single node *obj** and the tree *obj** of the two nodes after slicing. It traverses the slicing points of all the features and finds the slicing point of the largest *Gain*, which is the best splitting point. Through this process, the optimal transparency monitoring model can be obtained through the parameter design of the algorithm.

B. PEARSON CORRELATION COEFFICIENTS

Pearson Correlation Coefficients is a way to measure the correlation of variables [36]. Its output range is -1 to +1.0 means no correlation, negative value means negative correlation, and positive value means positive correlation. The larger the absolute value, the stronger the correlation. The calculation formula is:

$$r = \frac{\sum XY - \frac{\sum X \sum Y}{N}}{\sqrt{\left(\sum X^2 - \frac{(\sum X)^2}{N}\right)\left(\sum Y^2 - \frac{(\sum Y)^2}{N}\right)}} \quad (12)$$

where X represents the spectral characteristics of the sample points. In this experiment, it is the UAV-drone spectral value or the ratio characteristic of the band, Y represents the transparency value of the sample points, and N represents the number of samples.

C. MODEL ACCURACY EVALUATION

In this paper, the following statistical indicators were used to evaluate the transparency inversion models [37], [38].

1) MEAN ABSOLUTE ERROR (MAE)

The mean absolute error (MAE) can measure the stability of the model. The smaller the value, the more stable the model effect. The calculation formula is:

$$MAE = \frac{1}{n}\sum_{i=1}^{n}\left|\hat{y}_i - y_i\right| \quad (13)$$

where $\left|\hat{y}_i - y_i\right|$ represents the absolute error of the second result, and n is the number of samples in the test set. The value range of MAE is [0, $+\infty$). When the predicted value exactly matches the true value, it is equal to 0, which is the perfect model. The larger the error, the larger the MAE value.

2) ROOT-MEAN-SQUARE ERROR (RMSE)

The root-mean-square error (RMSE) is the square root of the ratio of the square of the deviation of the predicted value from the true value to the number of observations n. Its calculation formula is:

$$RMSE = \sqrt{\frac{1}{n}\sum_{i=1}^{n}\left(\hat{y}_i - y_i\right)^2} \quad (14)$$

The RMSE is very sensitive to extraordinarily large or very small errors in a set of data, so that it can reflect the accuracy of the prediction. The value range of RMSE is [0, $+\infty$).

3) R-SQUARED (R^2)

The R-squared value is used to characterize the quality of a fit through the change of data. Its calculation formula is:

$$R^2 = 1 - \frac{\sum\left(y_i - \hat{y}_i\right)^2}{\sum\left(y_i - \bar{y}\right)^2} \quad (15)$$

where $\bar{y}$ represents the average of the actual data set. In the formula, the denominator is the degree of dispersion of the original data, and the numerator is the error between the predicted value and the true value. Their ratio can eliminate the effect of the degree of dispersion of the original data. The closer R^2 is to 1, the better the ability of the equation's variables to explain y, and the model also fits the data better.

IV. RESULTS AND DISCUSSION

In total, 40 and 32 spectra were extracted from the UAV-borne hyperspectral images in the first research area of Shahu Port channel and the second research area of Xunsi River, respectively, with a band range of 400–1000 nm. The band range of 400–900 nm (225 bands) was cut to perform the transparency inversion experiments. As mentioned in the overview of the study area in Section II, the river water in the two study areas selected in this experiment is relatively turbid and has low visibility, so this experiment will not be affected by reflections from the bottom of the river. Correlation evaluation is an important part of the quantitative inversion modeling process. In the analysis of the experimental results, Pearson correlation coefficients were used to characterize the correlation between the drone spectrum X_Spectra and the inversion target Y_Transparency [39].

A. FIRST STUDY AREA: SHAHU PORT CHANNEL

This experiment involved the collection of transparency data for 40 sample points in the field at Shahu Port channel. The transparency distribution line chart is shown in Fig. 3. At sample point Nos. 1 to 13, the transparency is low, and the transparency values are less than 30cm, indicating that the water body in this section is relatively turbid and the visibility is poor. Sample point No. 3 has the lowest transparency at 19cm. After sample point No. 14, the transparency of the water body increases significantly, as a whole, with the transparency value of each sampling point being above 50 cm. The maximum value is sample point No. 16, for which the

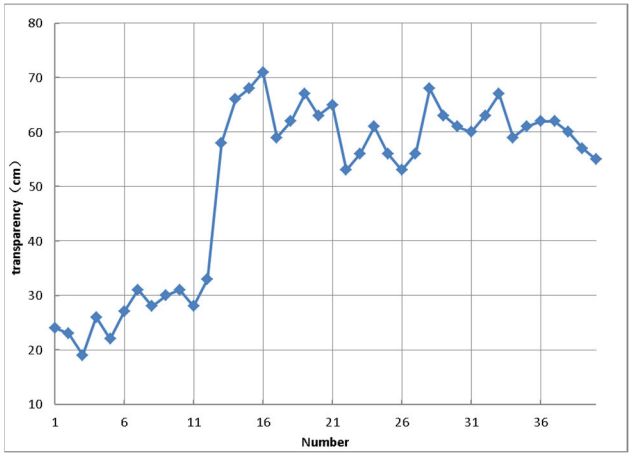

FIGURE 3. Shahu port channel transparency sampling results.

TABLE 2. Field transparency measurements from Shahu port channel.

Study area	Number of samples	Maximum value (cm)	Minimum value (cm)	Average value (cm)	Standard deviation (cm)
Shahu Port	40	71	19	50.85	16.34

transparency is 71cm. As shown in Table 2, the maximum value of the transparency of all the sampling points is 71cm, the minimum value is 19cm, the average value is 50.85cm, and the standard deviation is 16.34cm. Overall, the transparency of the 40 sample points at Shahu Port channel varies significantly.

The spectral curves extracted from the remote sensing imagery were pre-processed by the band ratio method, and Pearson correlation analysis was performed with the transparency values of the sampling points in the field. The correlation coefficients are shown in descending order in Fig. 4. The maximum correlation coefficient between the original remote sensing reflectance spectrum and the transparency

TABLE 3. Comparison of the modeling accuracy of the different traditional algorithms for the Shahu port channel data.

Method	Mathematical Model	Independent Variables	R^2	RMSE
Exponential function	$a \cdot \exp(b \cdot x)$	B136/B86	0.4459	12.4797
Power function	$a \cdot x^b$	B136/B86	0.6827	9.4432
Logarithmic function	$a \cdot \log(x) + b$	B136/B86	0.7954	7.5833
Linear function	$a \cdot x + b$	B136/B86	0.7953	7.5857
Quadratic polynomial	$a \cdot x^2 + b \cdot x + c$	B136/B86	0.7971	7.6532

TABLE 4. Comparison of the modeling accuracy of the different algorithms for the Shahu port channel data.

Method	Training data			Test data		
	R^2	RMSE (cm)	MAE (cm)	R^2	RMSE (cm)	MAE (cm)
GBDT	0.973	2.640	2.285	0.914	4.754	3.617
AdaBoost	0.986	1.908	1.423	0.975	2.545	2.001
Random Forest	0.976	2.477	1.970	0.970	2.806	1.983
XGBoost	0.988	1.711	1.306	0.976	2.515	2.008

is 0.72454 (Fig. 4a). Overall, the correlation coefficients of 76 spectra are greater than 0.6, which are mainly concentrated in the ranges of 400–430nm and 680–840nm, indicating that these band ranges are sensitive to changes in transparency.

The band ratio method can eliminate the interference of background noise, such as water surface smoothness and the surrounding environment, which changes temporally and spatially. This is a contrast enhancement operation commonly used in quantitative remote sensing inversion [40], [41]. In this experiment, the exhaustive method was used to

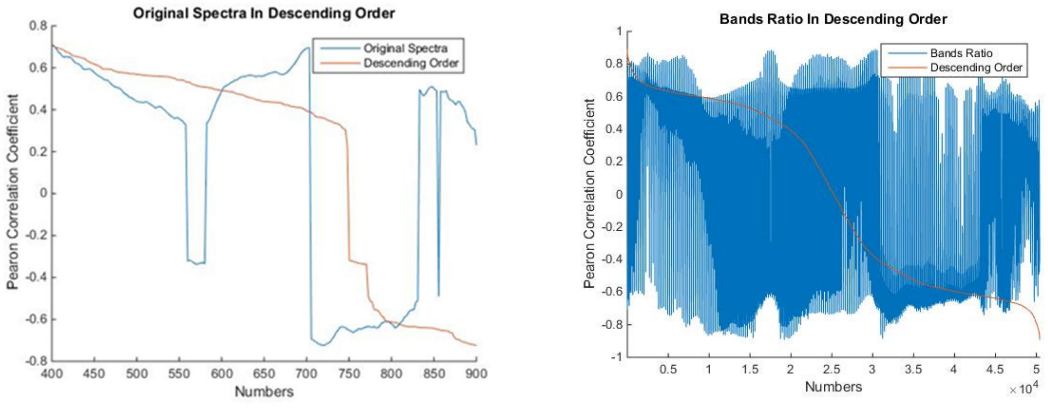

(a) (b)

FIGURE 4. Pearson correlation analysis with transparency. (a) Original spectra. (b) Band ratio result.

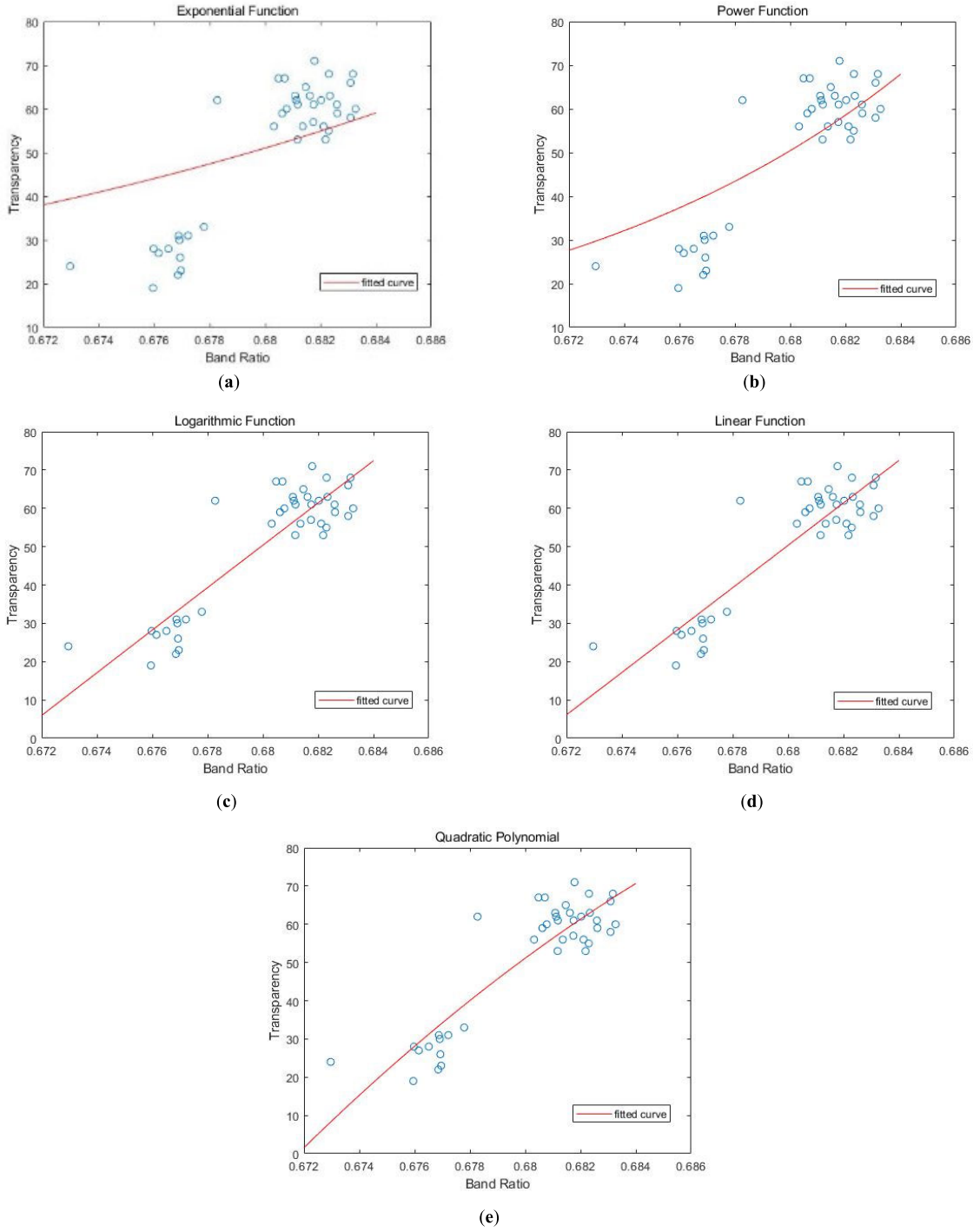

FIGURE 5. Fitted results of each function of Shahu Port: (a) Exponential function. (b) Power function. (c) Logarithmic function. (d) Linear function. (e) Quadratic polynomial.

calculate the ratio of the bands. The ratios of the 225 bands of the original spectra were calculated in pairs, and 50,400 characteristic variables were obtained. They are arranged in descending order according to the Pearson correlation coefficient as shown in Fig. 4b. The maximum correlation coefficient is 0.8918, and there are 312 remote sensing reflectance ratio correlation coefficients of greater than 0.8, with the maximum negative correlation being −0.8919. The correlation is significantly improved compared to the original spectra, so these data can be deemed as suitable for the transparency inversion modeling.

In this research, we tried to use the band ratio model to predict the transparency in various common remote sensing inversion models, including exponential function, power

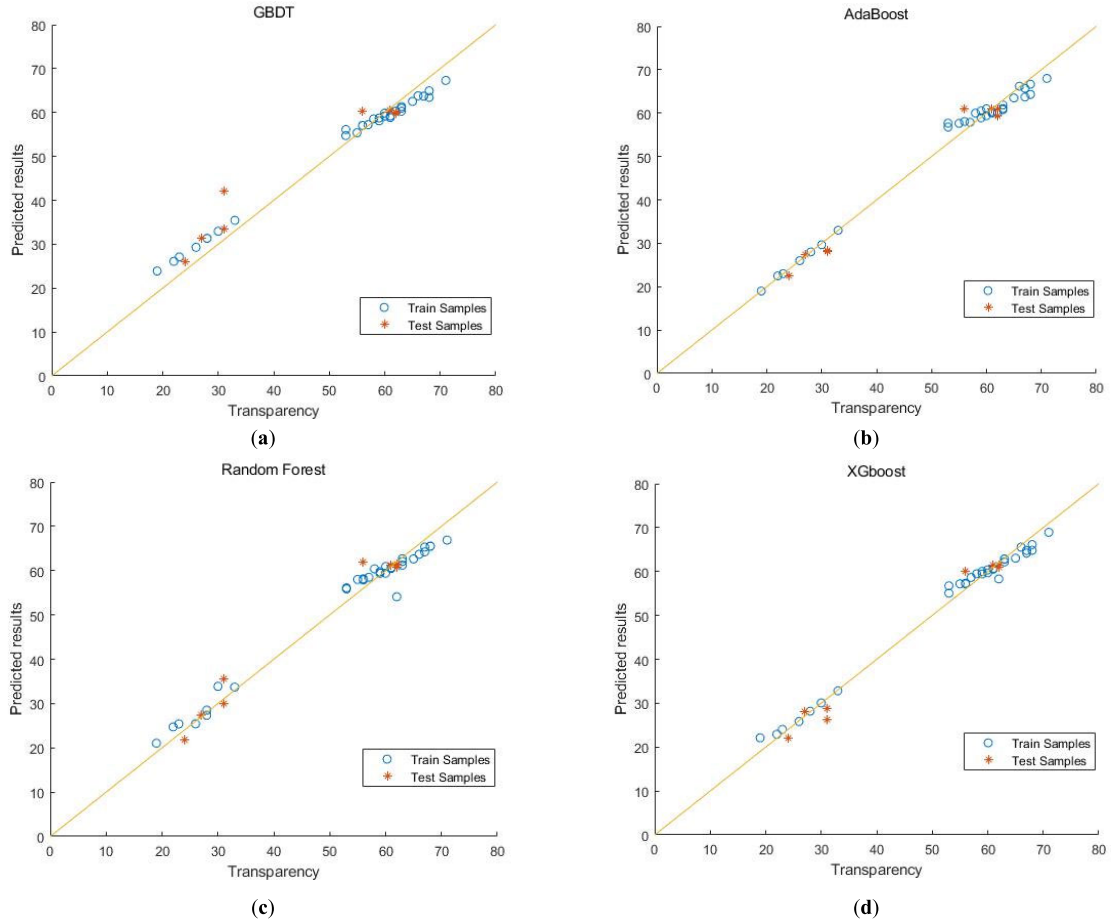

FIGURE 6. Relationship between the predicted and measured values of transparency with each method. (a) GBDT. (b) AdaBoost. (c) Random Forest. (d) XGBoost.

function, logarithmic function, linear function, and quadratic polynomial models to explore whether traditional methods are suitable for transparency inversion of urban rivers. In Shahu Port, the maximum correlation coefficient between the band ratio and the transparency ratio is 0.8919. The ratio (B136/B86) is the input variable of five empirical models, and the transparency is the output variable. The results of the inversion accuracy are listed in Table 3, and the fitted results are shown in Fig. 5. These results indicate that the traditional empirical models are not suitable for this experiment in Shahu Port.

Due to the small number of samples in this experiment, it is not necessary to set all the parameters when setting the parameters using the various integrated algorithms for the experiment. The parameters selected by GBDT for adjustment are learning_rate, the number of boosting stages to perform (n_estimators), and the fraction of samples used for fitting the individual base learners (subsample). The parameters that AdaBoost needs to set are n_estimators and learning rate. Random forest only needs to set the parameter n_estimators. The parameters required for XGBoost are n_estimators and maximum depth of the individual regression estimators (max_depth). Through the above three evaluation indexes RMSE, MAE and R^2, a suitable model is determined for the inversion of transparency.

When the GBDT parameter is set, n_estimators is set in units of 50, and it is finally determined to be 500. To prevent overfitting when setting the other two parameters learning_rate and subsample, the unit is 0.001 and 0.05 respectively, and it is finally determined to be 0.004 and 0.55. AdaBoost set parameters in accordance with GBDT, and finally determined that the parameters n_estimators is 100 and learning_rate is 0.001. When setting parameters in the random forest algorithm, n_estimators is in units of 50, and it is finally determined to be 100. When setting parameters in XGBoost, max_depth is in units of 1 and n_estimators is also in units of 50. Finally, it is determined that max_depth is 4 and n_estimators is 150.

From Table 4, comparing the inversion results of all the models for Shahu Port channel, XGBoost shows the best effect in predicting the transparency. Although the prediction accuracy for the XGBoost validation data set (R^2 = 0.976, RMSE = 2.515cm, MAE = 2.008cm) is lower than the prediction accuracy for the modeled data (R^2 = 0.988,

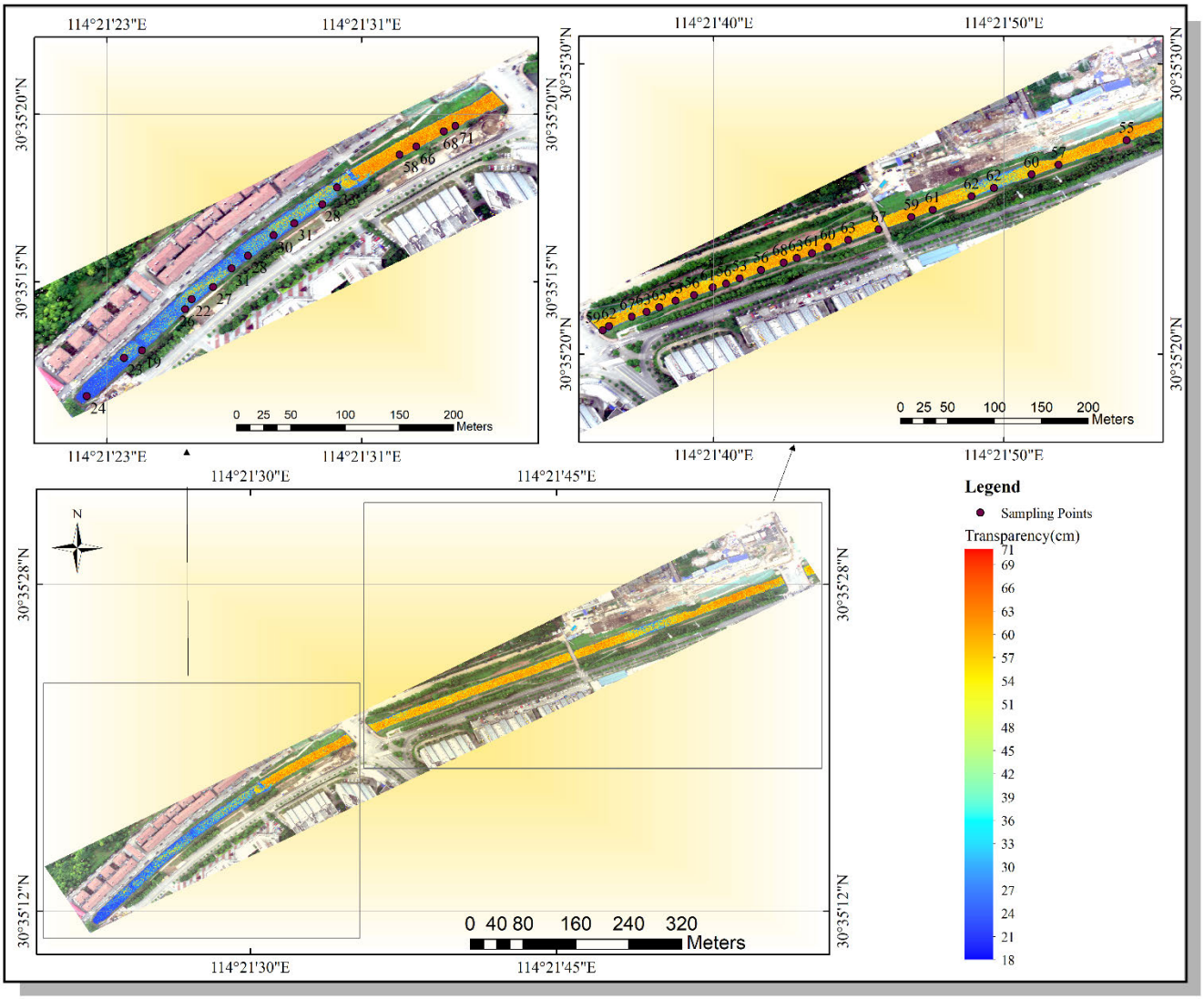

FIGURE 7. Inversion result map for Shahu port channel.

RMSE = 1.711cm, MAE = 1.306cm), on the basis of the minimum measured ground transparency of 19cm for Shahu Port channel, the inversion results meet the actual requirements.

In addition, the accuracy of the transparency inversion prediction of several other integrated methods for Shahu Port channel can also meet the actual needs. The modeling accuracy for the AdaBoost prediction model (R^2 = 0.986, RMSE = 1.908cm, MAE = 1.423cm) and the prediction accuracy for the validation set (R^2 = 0.975, RMSE = 2.545cm, MAE = 2.001cm) are slightly lower than the results of the XGBoost model, as a whole, but this model does obtain relatively good results. Compared with the AdaBoost model, the prediction accuracy of the random forest model is reduced, but it also obtains good prediction results, with the R^2 for the modeling set and the validation set reaching 0.97. Compared with the other methods, the prediction accuracy of the GBDT model in modeling the data (R^2 = 0.973, RMSE = 2.640cm, MAE = 2.285cm) is the same,

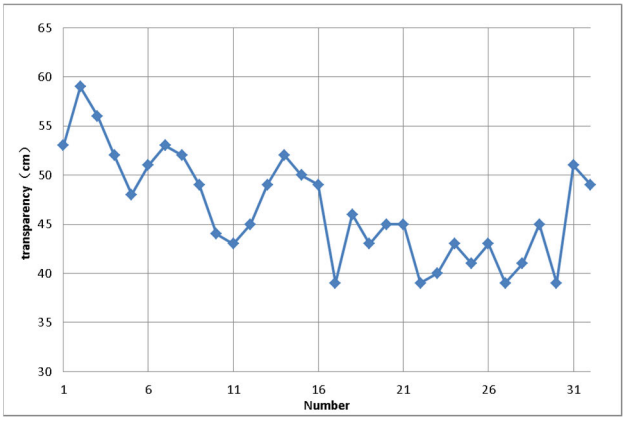

FIGURE 8. Xunsi river transparency sampling results.

but the prediction accuracy for the verification data (R^2 = 0.914, RMSE = 4.754cm, MAE = 3.617cm) decreases significantly. The inversion results of the training and test data

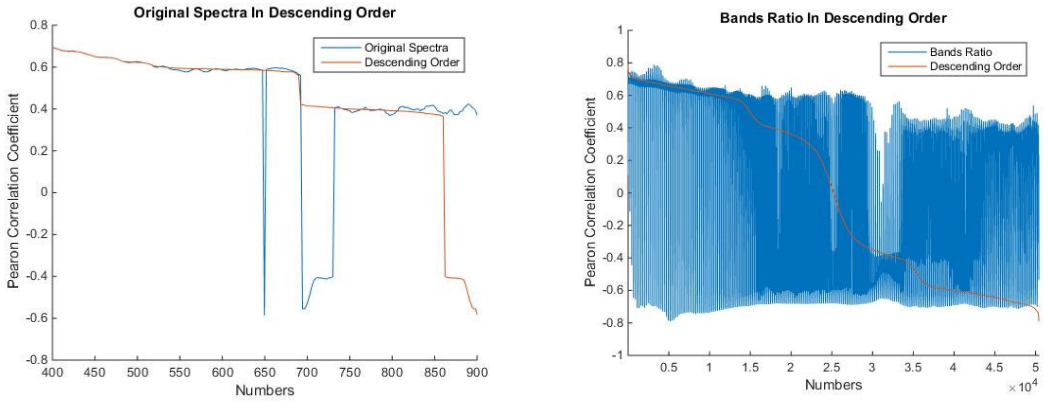

(a) (b)

FIGURE 9. Pearson correlation analysis with transparency. (a) Original spectra. (b) Band ratio result.

TABLE 5. Field transparency measurements from Xunsi river.

Study area	Number of samples	Maximum value (cm)	Minimum value (cm)	Average value (cm)	Standard deviation (cm)
Xunsi River	32	59	39	46.67	5.28

TABLE 6. Comparison of the modeling accuracy of the different traditional algorithms for the Xunsi river channel data.

Method	Mathematical Model	Independent Variables	R^2	RMSE
Exponential function	$a \cdot \exp(b \cdot x)$	B18/B25	0.5595	3.6033
Power function	$a \cdot x^b$	B18/B25	0.5612	3.5964
Logarithmic function	$a \cdot \log(x) + b$	B18/B25	0.5703	3.5587
Linear function	$a \cdot x + b$	B18/B25	0.5690	3.5641
Quadratic polynomial	$a \cdot x^2 + b \cdot x + c$	B18/B25	0.5919	3.5275

set are shown in Fig. 6. The predicted and true values of all samples are evenly distributed on the diagonal, indicating that the inversion results are good, and the model can be used for transparency inversion. Therefore, considering these results, the XGBoost model was selected for the inversion of the hyperspectral imagery of Shahu Port channel.

After saving the determined model and inputting the UAV-drone image, the inversion results of river transparency can be obtained. Fig. 7 shows the results of the inversion of the channel transparency with the hyperspectral imagery using the XGBoost model. According to the inversion results for Shahu Port channel, the maximum value of the inversion result is 70.27cm and the minimum value is 18.92cm. The maximum value of the field measurement of the transparency is 71cm and the minimum value is 19cm. The inversion results are therefore consistent with the actual results. The sampling points in Fig. 7 are marked with the transparency values measured in the field.

Further observation of the map shows that the distribution of the channel transparency is consistent with the results of the field sampling. The transparency distribution shows a trend of low first and then high. Before sampling point No. 12, most of the transparency is below 30cm. During the field sampling, this river section was quite turbid, the water body was black in color, and the pollution was serious. However, starting from the 13th point, the overall transparency increases significantly. Later field investigations revealed that the drainage outlet between points 12 and 13 is the drainage outlet for the nearby waterworks, from which treated purified water is discharged. Therefore, the transparency results for Shahu Port channel appear low at first and then high.

B. SECOND STUDY AREA: XUNSI RIVER

In this experiment, the transparency data for 32 sample points were collected in the field at Xunsi River. The line chart of the transparency distribution is shown in Fig. 8. In contrast with the results for Shahu Port channel, the transparency distribution of the sampling points for the Xunsi River is relatively stable, and the transparency values of each point are all between 35cm and 60cm. Statistics of the transparency information for the 32 sample points in Xunsi River are shown in Table 5. The maximum value of all the sample points is 59cm, the minimum value is 39cm, the average value is 46.67cm, and the standard deviation is 5.28cm. On the whole, the transparency of the sample points at Xunsi River changes only slightly. According to the preliminary judgment, there are no abnormal values in the transparency data from Xunsi River.

The spectral curves extracted from the UAV-borne remote sensing imagery were pre-processed by the band ratio method, and Pearson correlation analysis was performed with the transparency data of the field sampling points from Xunsi River. The correlation coefficients are shown in descending

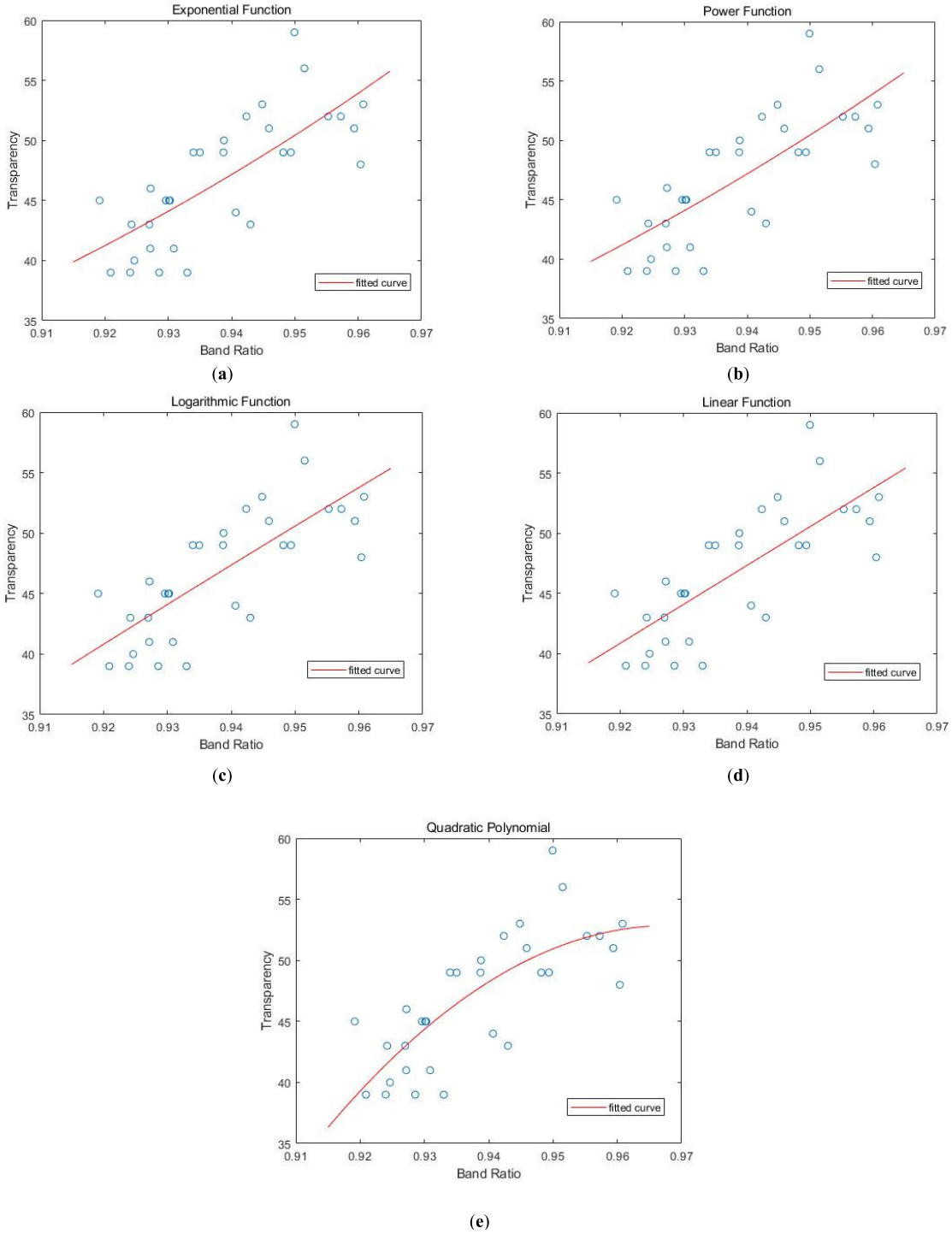

FIGURE 10. Fitted results of each function of Xunsi river: (a) Exponential function. (b) Power function. (c) Logarithmic function. (d) Linear function. (e) Quadratic polynomial.

order in Fig. 9. The maximum correlation coefficient between the original remote sensing reflectance spectra and the transparency is 0.6924 (Fig. 9a). Overall, 60 spectra have correlation coefficients of greater than 0.6, which are mainly concentrated in the 400–500nm range, indicating that this band range is sensitive to changes in transparency.

For the Xunsi River experiment, the band ratio enhancement was conducted again, which can eliminate the interference of background noise, such as water surface smoothness and the surrounding environment, which changes temporally and spatially. The exhaustive method was again used to calculate the ratios of the bands. The ratios of the 225 bands of

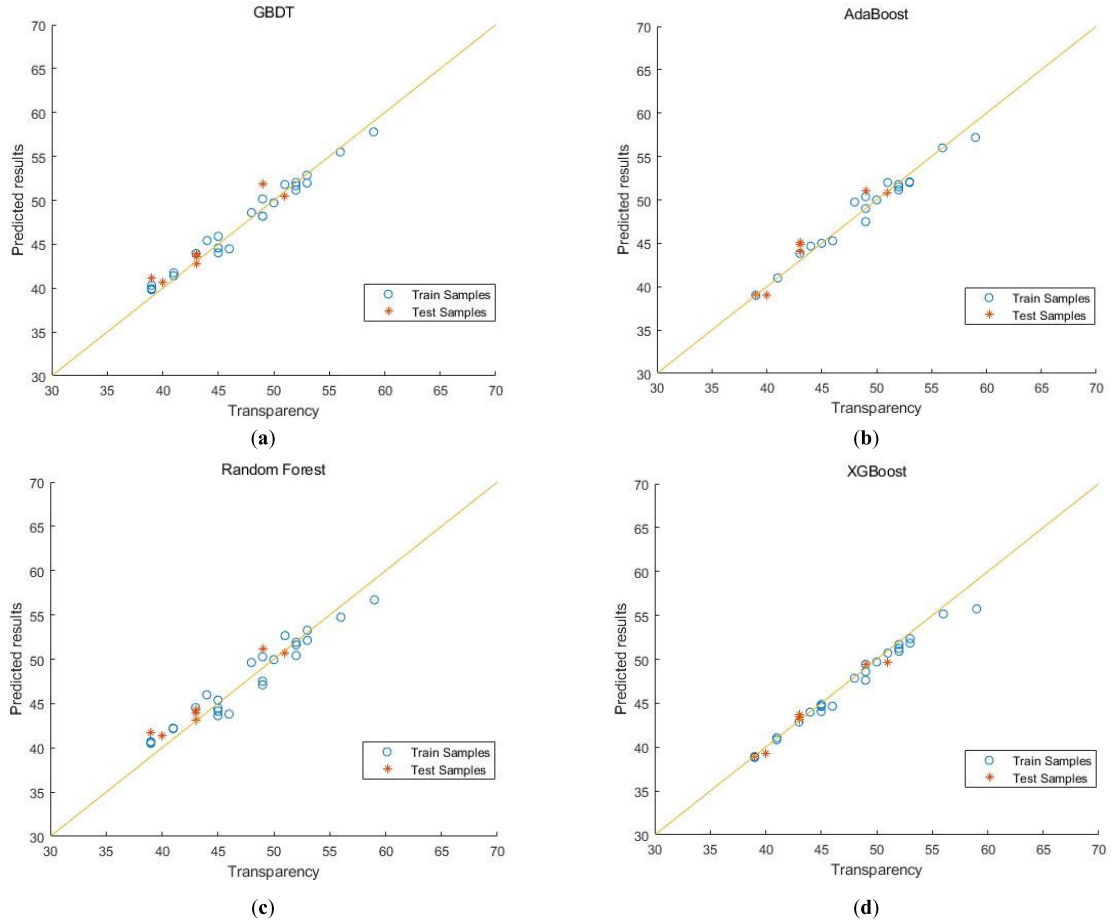

FIGURE 11. Relationship between the predicted and measured values of transparency with each method. (a) GBDT. (b) AdaBoost. (c) Random Forest. (d) XGBoost.

the original spectra were calculated in pairs, and 50,400 characteristic variables were obtained. The Pearson correlation coefficients and the transparency of the sample points are arranged in descending order in Fig. 9b. The maximum correlation coefficient is 0.7887. There are 47 remote sensing reflectance ratio correlation coefficients of greater than 0.75. The correlation is again significantly improved compared to the original spectra. Therefore, these data can be considered as suitable for the transparency inversion modeling.

In this experiment, we also used the band ratio model to predict the transparency in five common remote sensing inversion models. In Xunsi River, the maximum correlation coefficient between the band ratio and the transparency ratio is 0.7887. The ratio (B18/B25) is the input variable. The results of the inversion accuracy are listed in Table 6, and the fitted results are shown in Fig. 10. These results indicate that the traditional empirical models are not suitable for this experiment in Xunsi River.

When the GBDT parameter is set, n_estimators is set in units of, 50, and is finally determined to be 1500. To prevent overfitting when setting the learning_rate and subsample, it is set in units of 0.001 and 0.1 respectively, and it is finally determined to be 0.005 and 0.3. AdaBoost is similar to GBDT when setting parameters, and finally determined that the n_estimators is 400 and learning_rate is 0.001. When setting parameters in the random forest algorithm, n_estimators is also set to 50, which is finally determined to be 600. When setting parameters in XGBoost, max_depth is in units of 1 and n_estimators is also in units of 50. Finally, max_depth is determined to be 4 and n_estimators is 50.

From Table 7, comparing the inversion results of all the models for Xunsi River, XGBoost shows the best effect in predicting the transparency. For the Xunsi River research area, the prediction accuracy for the XGBoost validation data set (R^2 = 0.972, RMSE = 0.684cm, MAE = 0.561cm) is comparable to the prediction accuracy for the modeled data (R^2 = 0.971, RMSE = 0.901cm, MAE = 0.594cm). Based on the minimum measured transparency of 39cm and a standard deviation of 5.28cm on the ground for Xunsi River, the inversion results meet the experimental requirements.

In addition, the accuracy of the transparency inversion results of several other integrated methods for Xunsi River shows a significant decrease. The accuracy of the AdaBoost prediction model (R^2 = 0.976, RMSE = 0.799cm,

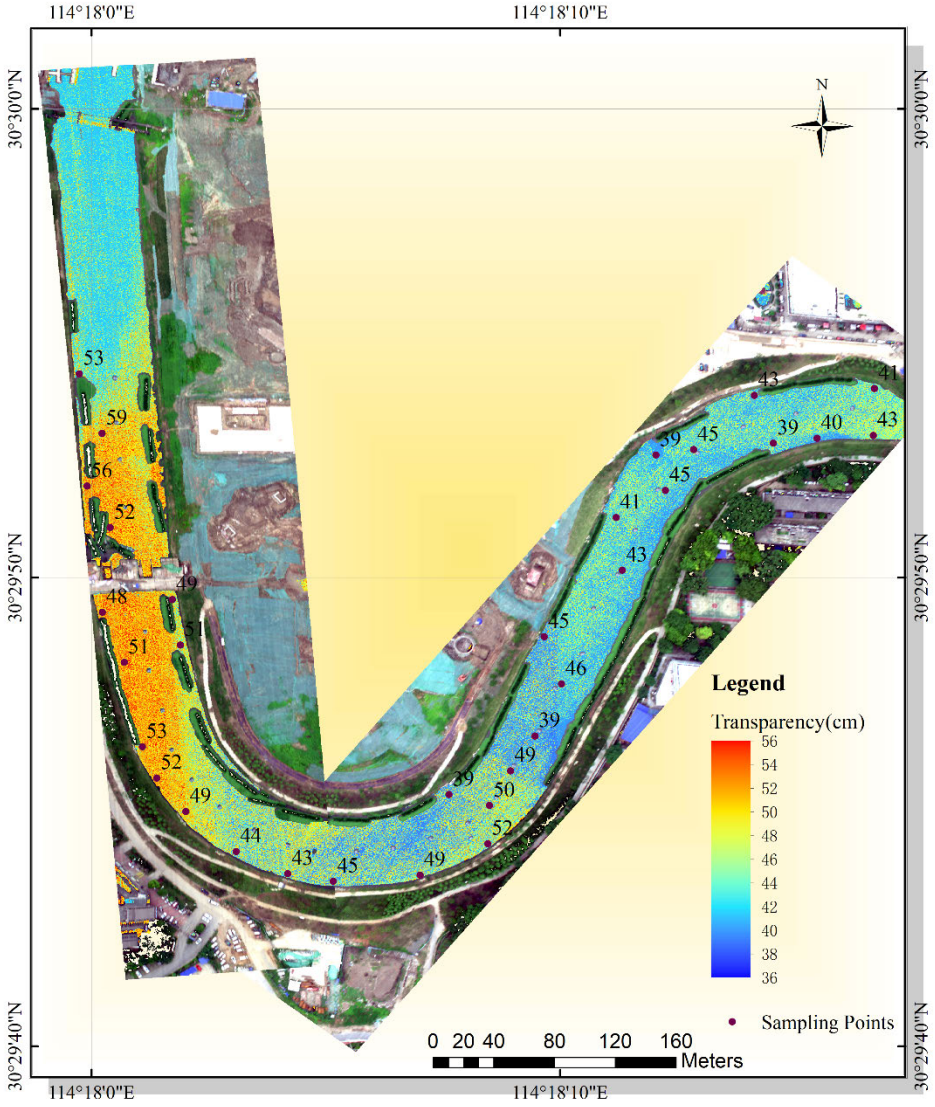

FIGURE 12. Inversion result map for Xunsi river.

MAE = 0.525cm) is improved, but the prediction accuracy for its validation data set (R^2 = 0.881, RMSE = 1.414cm, MAE = 1.165cm) decreases significantly, so these modeling results are not accurate enough. Similar to the AdaBoost model, the accuracy of the GBDT model (R^2 = 0.974, RMSE = 0.863cm, MAE = 0.774cm) is higher than the test set prediction accuracy (R^2 = 0.871, RMSE = 1.476cm, MAE = 1.152cm). Compared with the other methods, the prediction accuracy of the random forest model for the modeling data (R^2 = 0.932, RMSE = 1.386cm, MAE = 1.233cm) and the prediction accuracy for the verification data (R^2 = 0.858, RMSE = 1.548cm, MAE = 1.274cm) decrease significantly. The inversion results of the training and test data set are shown in Fig. 11. The predicted and true values of all samples are evenly distributed on the diagonal, indicating that the inversion results are good, and the model can be used for transparency inversion. Therefore, the XGBoost model was selected for the inversion of the hyperspectral imagery from Xunsi River.

TABLE 7. Comparison of the modeling accuracy of the different algorithms for the Xunsi river data.

Method	Training data			Test data		
	R^2	RMSE (cm)	MAE (cm)	R^2	RMSE (cm)	MAE (cm)
GBDT	0.974	0.863	0.774	0.871	1.476	1.152
AdaBoost	0.976	0.799	0.525	0.881	1.414	1.165
Random Forest	0.932	1.386	1.233	0.858	1.548	1.274
XGBoost	0.971	0.901	0.594	0.972	0.684	0.561

After the model parameters are determined, the inversion results can be obtained by inputting the UAV remote sensing images from the second study area. Fig. 12 shows the results of the XGBoost model's inversion of the transparency for the

Xunsi River hyperspectral imagery. According to the statistics of the inversion results for Xunsi River, the maximum value of the inversion result is 55.75cm and the minimum value is 37.95cm. The statistical results of the field measurement have a maximum value of 59cm and a minimum value of 39cm. Therefore, the inversion result is consistent with the actual result. The sampling points in Fig. 12 are marked with the transparency values measured in the field.

Further observation of the map shows that the distribution of the channel transparency for the Xunsi River is consistent with the results of the field sampling. The transparency distribution shows a trend of low, then high, and then low again. In conjunction with Fig. 2, it can be seen that, at sampling points Nos. 1 to 8, the transparency is mostly above 50cm. Upstream of these sampling points, it was observed during the field sampling that this river section was turbid and severely polluted. However, at the beginning, at sampling point No. 1, the overall transparency increases significantly. Later field investigations revealed that, between the No. 1 and No. 7 sampling points, green floating islands have been set up on both banks of the Xunsi River to purify the water. Green plants, including celery, are planted on the floating islands to purify the water [42]. Therefore, the transparency of Xunsi River appears to be low at first and then high. Because the distribution of the water quality is relatively uniform, this inversion result only reflects the distribution trend of the river transparency, and the prediction results at individual pixels are not considered here. When compared with the actual transparency measurement results, the inversion results can better reflect the transparency distribution trend of the river.

V. CONCLUSION

In this paper, we have described the quantitative inversion of UAV-borne hyperspectral imagery for urban river channel transparency monitoring. In the experiments undertaken in this study, the spectral data in the 400–900nm wavelength range of the hyperspectral imagery were extracted, and the original spectra were used to establish a band ratio model. Compared with five traditional empirical models and other boosting integrated algorithms, the accuracy of the water body transparency estimation using the XGBoost algorithm showed a significant improvement. And in the case of low overall transparency, the XGBoost algorithm works well in both research areas. The training and test set R^2 values in both study areas were higher than 0.97. Finally, the transparency inversion models were used to generate transparency distribution maps of the two study areas. The results confirmed that the distribution of the water transparency was consistent with the results of the field monitoring.

To date, there have been few studies of the application of UAV-borne hyperspectral imagery for water quality monitoring, and the algorithms used have been different. From the above discussion, it has been shown that integrated algorithms such as XGBoost have a high prediction accuracy when applied to the water quality monitoring of UAV-borne hyperspectral images, and the results can meet the actual needs. Therefore, in future research, such algorithms could be combined with UAV-borne hyperspectral imagery to monitor other water quality parameters, such as chlorophyll and suspended solids concentrations. This research involved using the rich features of UAV-borne hyperspectral imagery to build a statistical relationship with water transparency. Moreover, through this study, we confirmed that it is possible to use UAV-borne hyperspectral imagery to achieve the dynamic monitoring of urban river water quality. With the immediacy of UAV-drone data acquisition, this research can be applied in more aspects, such as pollution source monitoring and pollutant transfer. In our future research, we will attempt to make better use of the hyperspectral spectral features.

ACKNOWLEDGMENT

The Intelligent Data Extraction and Remote Sensing Analysis Group of Wuhan University (RSIDEA) provided the datasets. The Remote Sensing Monitoring and Evaluation of Ecological Intelligence Group (RSMEEI) helped to process the datasets.

REFERENCES

[1] Y. Wu, L. Guo, Z. Xia, P. Jing, and X. Chunyu, "Reviewing the Poyang lake hydraulic project based on humans' changing cognition of water conservancy projects," *Sustainability*, vol. 11, no. 9, p. 2605, May 2019, doi: 10.3390/su11092605.

[2] T. J. Malthus, E. L. Hestir, A. G. Dekker, and V. E. Brando, "The case for a global inland water quality product," in *Proc. IEEE Int. Geosci. Remote Sens. Symp.*, Jul. 2012, p. 5.

[3] S. Bai, J. Gao, D. Sun, and M. Tian, "Monitoring water transparency in shallow and eutrophic lake waters based on GOCI observations," *Remote Sens.*, vol. 12, no. 1, p. 163, Jan. 2020, doi: 10.3390/rs12010163.

[4] L. Feng, X. Hou, and Y. Zheng, "Monitoring and understanding the water transparency changes of fifty large lakes on the yangtze plain based on long-term MODIS observations," *Remote Sens. Environ.*, vol. 221, pp. 675–686, Feb. 2019, doi: 10.1016/j.rse.2018.12.007.

[5] M. Karydis, "Eutrophication assessment of coastal waters based on indicators: A literature review," *Global NEST J.*, vol. 11, no. 4, pp. 373–390, Apr. 2013, doi: 10.30955/gnj.000626.

[6] M. M. Squires, L. F. W. Lesack, and D. Huebert, "The influence of water transparency on the distribution and abundance of macrophytes among lakes of the Mackenzie delta, Western Canadian arctic," *Freshwater Biol.*, vol. 47, no. 11, pp. 2123–2135, Nov. 2002, doi: 10.1046/j.1365-2427.2002.00959.x.

[7] A. Vundo, B. Matsushita, D. Jiang, M. Gondwe, R. Hamzah, F. Setiawan, and T. Fukushima, "An overall evaluation of water transparency in lake malawi from MERIS data," *Remote Sens.*, vol. 11, no. 3, p. 279, Jan. 2019, doi: 10.3390/rs11030279.

[8] A.-M. Schwarz and I. Hawes, "Effects of changing water clarity on characean biomass and species composition in a large oligotrophic lake," *Aquatic Botany*, vol. 56, nos. 3–4, pp. 169–181, Apr. 1997, doi: 10.1016/S0304-3770(96)01114-X.

[9] E. S. Al-Kharusi, D. E. Tenenbaum, A. M. Abdi, T. Kutser, J. Karlsson, A.-K. Bergström, and M. Berggren, "Large-scale retrieval of coloured dissolved organic matter in northern lakes using Sentinel-2 data," *Remote Sens.*, vol. 12, no. 1, p. 157, Jan. 2020, doi: 10.3390/rs12010157.

[10] R. Portielje and D. T. Van der Molen, "Relationships between eutrophication variables: from nutrient loading to transparency," in *Shallow Lakes*, N. Walz B. Nixdorf, Eds. Dordrecht, The Netherlands:: Springer, 1999, pp. 375–387.

[11] Z. Lee, S. Shang, C. Hu, K. Du, A. Weidemann, W. Hou, J. Lin, and G. Lin, "Secchi disk depth: A new theory and mechanistic model for underwater visibility," *Remote Sens. Environ.*, vol. 169, pp. 139–149, Nov. 2015, doi: 10.1016/j.rse.2015.08.002.

[12] N.-B. Chang, S. Imen, and B. Vannah, "Remote sensing for monitoring surface water quality status and ecosystem state in relation to the nutrient cycle: A 40-year perspective," *Crit. Rev. Environ. Sci. Technol.*, vol. 45, no. 2, pp. 101–166, Jan. 2015, doi: 10.1080/10643389.2013.829981.
[13] K. Dörnhöfer and N. Oppelt, "Remote sensing for lake research and monitoring–Recent advances," *Ecol. Indicators*, vol. 64, pp. 105–122, May 2016, doi: 10.1016/j.ecolind.2015.12.009.
[14] X. He, D. Pan, and Z. Mao, "Water-transparency (Secchi Depth) monitoring in the China Sea with the SeaWiFS satellite sensor," *Proc. SPIE*, vol. 5568, p. 112, Oct. 2004 doi: 10.1117/12.564605.
[15] N. Li, K. Shi, Y. Zhang, Z. Gong, K. Peng, Y. Zhang, and Y. Zha, "Decline in transparency of lake hongze from long-term MODIS observations: Possible causes and potential significance," *Remote Sens.*, vol. 11, no. 2, p. 177, Jan. 2019, doi: 10.3390/rs11020177.
[16] M. Bonansea, R. Bazán, C. Ledesma, C. Rodriguez, and L. Pinotti, "Monitoring of regional lake water clarity using landsat imagery," *Hydrol. Res.*, vol. 46, no. 5, pp. 661–670, Oct. 2015, doi: 10.2166/nh.2014.211.
[17] T. Kouts, L. Sipelgas, N. Savinits, and U. Raudsepp, "Environmental monitoring of water quality in coastal sea area using remote sensing and modeling," in *Proc. IEEE US/EU Baltic Int. Symp.*, Klaipeda, Lithuania, May 2006, pp. 1–8, doi: 10.1109/BALTIC.2006.7266166.
[18] J. C. Ritchie, P. V. Zimba, and J. H. Everitt, "Remote sensing techniques to assess water quality," *Photogrammetric Eng. Remote Sens.*, vol. 69, no. 6, pp. 695–704, Jun. 2003, doi: 10.14358/PERS.69.6.695.
[19] F. Setiawan, B. Matsushita, R. Hamzah, D. Jiang, and T. Fukushima, "Long-term change of the secchi disk depth in lake maninjau, indonesia shown by landsat TM and ETM+ data," *Remote Sens.*, vol. 11, no. 23, p. 2875, Dec. 2019, doi: 10.3390/rs11232875.
[20] S. Thiemann and H. Kaufmann, "Lake water quality monitoring using hyperspectral airborne data—A semiempirical multisensor and multitemporal approach for the Mecklenburg Lake District, Germany," *Remote Sens. Environ.*, vol. 81, nos. 2–3, pp. 228–237, Aug. 2002, doi: 10.1016/S0034-4257(01)00345-5.
[21] R. J. Allee and J. E. Johnson, "Use of satellite imagery to estimate surface chlorophyll a and secchi disc depth of bull shoals reservoir, Arkansas, USA," *Int. J. Remote Sens.*, vol. 20, no. 6, pp. 1057–1072, Jan. 1999, doi: 10.1080/014311699212849.
[22] S. M. Kloiber, P. L. Brezonik, and M. E. Bauer, "Application of Landsat imagery to regional-scale assessments of Lake Clarity," *Water Res.*, vol. 36, no. 17, pp. 4330–4340, Oct. 2002, doi: 10.1016/S0043-1354(02)00146-X.
[23] K. E. Sawaya, L. G. Olmanson, N. J. Heinert, P. L. Brezonik, and M. E. Bauer, "Extending satellite remote sensing to local scales: Land and water resource monitoring using high-resolution imagery," *Remote Sens. Environ.*, vol. 88, nos. 1–2, pp. 144–156, Nov. 2003, doi: 10.1016/j.rse.2003.04.006.
[24] P. W. Mausel, M. A. Karaska, C. Y. Mao, D. E. Escobar, and J. H. Everitt, "Insights into secchi transparency through computer analysis of aerial multispectral video data," *Int. J. Remote Sens.*, vol. 12, no. 12, pp. 2485–2492, Dec. 1991, doi: 10.1080/01431169108955282.
[25] M. Gholizadeh, A. Melesse, and L. Reddi, "A comprehensive review on water quality parameters estimation using remote sensing techniques," *Sensors*, vol. 16, no. 8, p. 1298, Aug. 2016, doi: 10.3390/s16081298.
[26] C. C. Trees, "Monitoring water transparency and diver visibility in ports and harbors using aircraft hyperspectral remote sensing," *Proc. SPIE*, vol. 5780, p. 91, May 2005, doi: 10.1117/12.607554.
[27] Wei, Huang, Wang, Wang, Zhou, and Cao, "Monitoring of urban black-odor water based on nemerow index and gradient boosting decision tree regression using UAV-borne hyperspectral imagery," *Remote Sens.*, vol. 11, no. 20, p. 2402, Oct. 2019, doi: 10.3390/rs11202402.
[28] J. Tang, G. Tian, X. Wang, X. Wang, and Q. Song, "The methods of water spectra measurement and analysis I: Above-water method," *J. Remote Sens.*, vol. 8, no. 1, pp. 37–44, Jan. 2004.
[29] L. Wei, C. Huang, Y. Zhong, Z. Wang, X. Hu, and L. Lin, "Inland waters suspended solids concentration retrieval based on PSO-LSSVM for UAV-borne hyperspectral remote sensing imagery," *Remote Sens.*, vol. 11, no. 12, p. 1455, Jun. 2019, doi: 10.3390/rs11121455.
[30] Y. Lee, D. Han, M.-H. Ahn, J. Im, and S. J. Lee, "Retrieval of total precipitable water from Himawari-8 AHI data: A comparison of random forest, extreme gradient boosting, and deep neural network," *Remote Sens.*, vol. 11, no. 15, p. 1741, Jul. 2019, doi: 10.3390/rs11151741.
[31] T. Chen and C. Guestrin, "XGBoost: A scalable tree boosting system," in *Proc. 22nd ACM SIGKDD Int. Conf. Knowl. Discovery Data Mining*, Aug. 2016, pp. 785–794, doi: 10.1145/2939672.2939785.
[32] S. Oliveira, F. Oehler, J. San-Miguel-Ayanz, A. Camia, and J. M. C. Pereira, "Modeling spatial patterns of fire occurrence in Mediterranean Europe using multiple regression and random forest," *Forest Ecol. Manage.*, vol. 275, pp. 117–129, Jul. 2012, doi: 10.1016/j.foreco.2012.03.003.
[33] D. Brzezinski and J. Stefanowski, "Reacting to different types of concept drift: The accuracy updated ensemble algorithm," *IEEE Trans. Neural Netw. Learn. Syst.*, vol. 25, no. 1, pp. 81–94, Jan. 2014, doi: 10.1109/TNNLS.2013.2251352.
[34] D. P. Solomatine and D. L. Shrestha, "AdaBoost.RT: A boosting algorithm for regression problems," in *Proc. IEEE Int. Joint Conf. Neural Netw.*, vol. 2. Budapest, Hungary, Jul. 2004, pp. 1163–1168, doi: 10.1109/IJCNN.2004.1380102.
[35] J. Wang, P. Li, R. Ran, Y. Che, and Y. Zhou, "A short-term photovoltaic power prediction model based on the gradient boost decision tree," *Appl. Sci.*, vol. 8, no. 5, p. 689, Apr. 2018, doi: 10.3390/app8050689.
[36] J. Wang, "Pearson correlation coefficient," in *Encyclopedia of Systems Biology*, W. Dubitzky, O. Wolkenhauer, K.-H. Cho, H. Yokota, Eds. New York, NY, USA: Springer, 2013, p. 1671.
[37] T. Chai and R. R. Draxler, "Root mean square error (RMSE) or mean absolute error (MAE)?" *Geoscientific Model Develop. Discuss.*, vol. 7, no. 1, pp. 1525–1534, Feb. 2014, doi: 10.5194/gmdd-7-1525-2014.
[38] T. Zhang and F. Frank, "An approach to improving the retrieval accuracy of oceanic constituents in case II waters," *J. Ocean Univ. China*, vol. 3, no. 2, pp. 220–224, Oct. 2004, doi: 10.1007/s11802-004-0038-3.
[39] P. Sedgwick, "Pearson's correlation coefficient," *BMJ*, vol. 345, p. e4483, Jul. 2012, doi: 10.1136/bmj.e4483.
[40] K. Danquah and T. Brunclík, "Band ratio model for remotely estimating water quality parameters in small inland water bodies based on Landsat ETM+ data," *Sci. Papers Univ. Pardubice, Ser. A*, vol. 24, pp. 167–185, Oct. 2018.
[41] M. Niroumand-Jadidi and A. Vitti, "Optimal band ratio analysis of worldview-3 imagery for bathymetry of shallow rivers (case study: Sarca River, Italy)," *ISPRS-Int. Arch. Photogramm., Remote Sens. Spatial Inf. Sci.*, vols. XLI–B8, pp. 361–364, Jun. 2016, doi: 10.5194/isprs-archives-XLI-B8-361-2016.
[42] W. Chen, J. Zheng, Z. Li, G. Shen, and Y. Li, "Status of water environment pollution in the xixi wetland and its ecological treatment countermeasures," *Frontiers Biol. China*, vol. 4, no. 2, pp. 228–232, Jun. 2009, doi: 10.1007/s11515-009-0004-y.

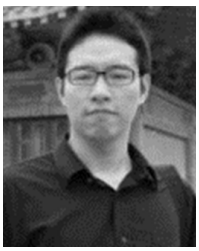

LIFEI WEI received the Ph.D. degree in photogrammetry and remote sensing from the State Key Laboratory of Information Engineering in Surveying, Mapping, and Remote Sensing, Wuhan University, China, in 2011. He is currently an Associate Professor with Hubei University, China. His major research interests include remote sensing image processing, ecological remote sensing, and agricultural remote sensing.

ZHOU WANG received the B.S. degree in geographical information science from Hubei University, Wuhan, China, in 2018, where he is currently pursuing the M.S. degree in cartography and geographic information system with the Faculty of Resources and Environmental Science. His major research interests include UAV-borne hyperspectral, and remote sensing in water pollution.

CAN HUANG received the B.S. degree in computer science and the M.S. degree in cartography and geographic information system from the Faculty of Resources and Environmental Science, Hubei University, Wuhan, China, in 2017 and 2020, respectively. His major research interests include unmanned aerial vehicle-borne hyperspectral remote sensing, and image classification.

YU ZHANG received the B.S. degree in geography and the M.S. degree in cartography and geographic information system from the Faculty of Resources and Environmental Science, Hubei University, Wuhan, China. in 2017 and 2020, respectively. Her major research interests include unmanned aerial vehicle-borne hyperspectral remote sensing, and agricultural remote sensing.

ZHENGXIANG WANG received the M.S. degree in botany from Central China Normal University, Wuhan, China, in 2000, and the Ph.D. degree in life environment from Yokohama National University, Japan, in 2004. He is currently the Head of the Faculty of Resources and Environmental Science, Hubei University, Wuhan, China. His major research interests include vegetation ecology and biodiversity conservation.

HUIQIONG XIA received the M.S. degrees in photogrammetry and remote sensing from Wuhan University, Wuhan, China, in 2005 and 2009, respectively. She is currently an Associate Professor with the Faculty of Resources and Environmental Science, Hubei University, Wuhan, China. Her research interests include spatiotemporal data modeling, and 3D modeling.

LIQIN CAO (Member, IEEE) received the M.S. and Ph.D. degrees in photogrammetry and remote sensing from Wuhan University, Wuhan, China, in 2006 and 2009, respectively. From 2015 to 2016, she was a Visiting Research Fellow with the Department of Information and Communication Technology, University of Agder (UiA), Grimstad, Norway. She is currently with the School of Printing and Packaging, Wuhan University. Her research interests include image processing, computer vision, and remote sensing data processing.